

# The Size, Structure and Ionization of the Broad Line Region in NGC 3227

Nick Devereux

*Department of Physics, Embry-Riddle Aeronautical University, Prescott, AZ 86301*

devereux@erau.edu

## ABSTRACT

*Hubble Space Telescope* spectroscopy of the Seyfert 1.5 galaxy, NGC 3227, confirms previous reports that the broad H $\alpha$  emission line flux is time variable, decreasing by a modest  $\sim 11\%$  between 1999 and 2000 in response to a corresponding  $\sim 37\%$  decrease in the underlying continuum. Modeling the gas distribution responsible for the broad H $\alpha$ , H $\beta$  and H $\gamma$  emission lines favors a spherically symmetric inflow as opposed to a thin disk. Adopting a central black hole mass of  $7.6 \times 10^6 M_{\odot}$ , determined from prior reverberation mapping, leads to the following dimensions for the size of the region emitting the broad H $\alpha$  line; an outer radius  $\sim 90$  l.d and an inner radius  $\sim 3$  l.d. Thus, the previously determined reverberation size for the broad line region (BLR) consistently coincides with the inner radius of a much *larger* volume of ionized gas. However, the *perceived* size of the BLR is an illusion, a consequence of the fact that the emitting region is ionization bounded at the outer radius and diminished by Doppler broadening at the inner radius. The actual dimensions of the inflow remain to be determined. Nevertheless, the steady state mass inflow rate is estimated to be  $\sim 10^{-2} M_{\odot} \text{ yr}^{-1}$  which is sufficient to explain the X-ray luminosity of the AGN in terms of radiatively inefficient accretion. Collectively, the results challenge many preconceived notions concerning the nature of BLRs in active galactic nuclei.

*Subject headings:* galaxies: Seyfert, galaxies: individual (NGC 3227), quasars: emission lines

## 1. Introduction

NGC 3227 is an early type SAB(s)a spiral galaxy located at a distance of 20.8 Mpc (Tully 1988). The galaxy harbors a Seyfert 1.5 nucleus (Ho, Filippenko, Sargent & Peng

1997) whose broad Balmer emission lines have long been known to be time variable. Since the broad line region (BLR) is unresolved, the spatial distribution of emission cannot be directly measured. However, reverberation mapping, which refers to measuring the time delay in the response of broad emission lines to time variable illumination from the central continuum source (Peterson 1993), has yielded a variety of estimates for the size of the broad line region (Peterson, Crenshaw & Meyers 1985; Winge et al. 1995; Peterson et al. 2004; Kaspi et al. 2005; Denney et al. 2009, 2010). Even though the broad line emission emanates from a finite volume, reverberation mapping yields only a single size. Despite numerous attempts to model the reverberation phenomenon (e.g., Edelson & Krolik 1988; Robinson & Perez 1990; Welsh & Horne 1991; Horne, Peterson, Collier, & Netzer 2004; Korista & Goad 2004; Pancoast, Brewer & Treu 2011, and references therein), the question remains *what exactly does the reverberation size refer to; the inner radius of the BLR, the outer radius or a luminosity weighted radius?*

Emission line profile fitting is a complementary technique used to constrain the physical dimensions of the BLR in low luminosity AGNs (LLAGNs) with known central masses. Gravity dominates the kinematics of the gas because LLAGNs radiate well below the Eddington limit with insufficient radiation pressure to drive an outflow. Consequently, knowing the relationship between velocity and radius allows the broad emission line profiles to be modeled revealing the shape and size of the BLR. This technique has led to large BLR size discrepancies for the LLAGNs M81, NGC 3998 and NGC 4203 (Devereux & Shearer 2007; Devereux 2011a,b). Specifically, the dimensions of the BLR deduced from emission line profile fitting are much larger than expected based on the reverberation size–UV luminosity correlation of Kaspi et al. (2005). However, Kaspi et al. (2005) note that the correlation appears to break down for AGNs with low UV luminosities, comparable to those measured for M81, NGC 3998 and NGC 4203, so the comparison may not be meaningful. On the other hand, the reverberation size has actually been measured for the LLAGN in NGC 3227, most recently by Denney et al. (2010). The principle aim of this paper, therefore, is to make the first direct comparison of the reverberation size with the dimensions of the BLR in NGC 3227 deduced from emission line profile fitting. The larger context for this investigation is to understand why it is that BH masses estimated using the reverberation radius require a considerable factor of  $\sim 5.5$  correction in order to place them on the  $M_{\bullet}-\sigma_{*}$  relation defined by BH masses measured directly using gas and stellar kinematics (Onken et al. 2004).

The mass of the BH in NGC 3227 has been measured using three different methods; stellar kinematics (Davies et al. 2006), gas kinematics (Hicks & Malkan 2008) and most recently via reverberation mapping (Denney et al. 2010), collectively yielding mass estimates in the range  $(0.7 - 2) \times 10^7 M_{\odot}$ . When combined with the X-ray luminosity the range of BH masses indicate that NGC 3227 is radiating at  $\leq 0.4\%$  of the Eddington luminosity limit

(Winter, Veilleux, McKernan & Kallman 2011; Xu 2011; Vasudevan & Fabian 2009).

The layout of the paper is as follows. In Section 3, the broad emission lines seen in NGC 3227 are evaluated in the context of inflow and accretion disk models. Some physical properties of the BLR are presented in Section 4 including the size, structure and source of ionization. Conclusions follow in Section 5. We begin, however, with Section 2 and a review of the emission lines observed in the nucleus of NGC 3227.

## 2. NGC 3227 Emission Lines

NGC 3227 has been observed with STIS twice; once in 1999 with the G750M grating and again in 2000 with the G750L, G430L, G230L and G140L gratings. Table 1 summarizes the observations and the archival spectra are presented in Figure 1. STIS spectra showing the UV–visible emission have been presented previously; Crenshaw, Kraemer, Bruhweiler, & Ruiz (2001) based on observations obtained under PID 8479 and the G750M spectrum obtained under PID 7403, by Walsh et al. (2008). All spectra shown in the following refer to a 7 pixel wide extraction along the slit direction and centered on the nucleus. Each extraction samples  $\geq 80\%$  of the encircled energy for an unresolved point source (Proffitt et al. 2010). It is quite obvious from the G750M and G750L spectra that the continuum decreased in brightness by  $\sim 37\%$  between 1999 and 2000. Collectively, the G750M, G750L and G430L spectra resolve the  $H\alpha$ ,  $H\beta$  and  $H\gamma$  lines, a more detailed description of which follows in the next section.

### 2.0.1. Broad Balmer line Emission

Figure 2 illustrates that  $H\alpha$  emission line profile is single peaked and both of the [N II] vacuum wavelength 6549.85 Å and 6585.28 Å emission lines can be seen in the high resolution G750M spectrum facilitating their ultimate subtraction to reveal an unadulterated broad  $H\alpha$  emission line. That the tips of the [N II] lines are clearly visible provides a useful constraint on their flux. Rather than constraining the width of the [N II] lines to be the same as the [S II] lines (e.g., Noel–Storr et al. 2003; Walsh et al. 2008), the width and the flux of the brightest [N II] line, and by association the fainter [N II] line, were determined empirically by selecting the values that resulted in the *cleanest* subtraction. Persistent irregularities in the broad  $H\alpha$  emission line profile may be real as they do not coincide with the central wavelengths of the subtracted [N II] lines as illustrated in Figure 2. Otherwise, the broad  $H\alpha$  emission line profile is symmetric about the  $\lambda 6588\text{Å}$  wavelength expected for a systemic

velocity of 1126 km/s deduced from the peak of the brightest [N II] emission line. Thus, there is no apparent redshift between the broad H $\alpha$  emission line and the systemic redshift of the host galaxy. The **STSDAS** contributed task **specfit** was used to model and subtract the forbidden lines and the results are reported in Table 2 along with the fluxes for the two [S II] vacuum wavelength  $\lambda 6718.29$  and  $\lambda 6732.67$  Å emission lines and the two [O I] vacuum wavelength  $\lambda 6302.04$  and  $\lambda 6365.53$  Å emission lines.

It is also customary to subtract a narrow component of the H $\alpha$  line. This practice arose because the relatively large, 1 - 2 arc sec wide, slits employed for ground based spectroscopic observations (e.g., Ho, Filippenko & Sargent 1996) inevitably included “extended” narrow line gas leading to a narrow component of H $\alpha$  emission centered at the systemic velocity of the galaxy. However, the STIS spectra examined in this paper were obtained with a much smaller 0.2 arc sec slit (Table 1) and subsequent modeling shows that the H $\alpha$  emission originates from an even smaller region, less than  $5 \times 10^{-4}$  arc sec in radius (§4.2, 4.3). Consequently, there is no evidence for an “extended” narrow line region of H emitting gas. Besides, estimating the flux of the narrow H $\alpha$  line is highly subjective. The model employed by Walsh et al. (2008) for NGC 3227 has the narrow H $\alpha$  brighter than the brightest [N II] line whereas the narrow H $\alpha$  line is typically *observed* to be 3 to 5 times fainter than the brightest [N II] line in STIS spectra of AGNs for which the lines can be clearly seen (e.g., Noel-Storr et al. 2003). Furthermore, it can be demonstrated empirically that subtracting a narrow H $\alpha$  component with less than half the flux of the brightest [N II] line has little consequence on the appearance of the bright central spike in the G750M spectrum. Also, in the specific case of NGC 3227, presumably the H $\beta$  and H $\gamma$  profiles have central spikes as well, but there is no way to see them and subtract them with the low resolution spectra that are currently available. Under these circumstances it would be inappropriate to subtract a narrow component from the H $\alpha$  line and not the other Balmer lines as well. Another important consideration to bear in mind is that a bright central spike is a feature of an inflow just as double peaks are a feature of a disk (e.g., Chen & Halpern 1989) and to subtract the bright spike from the H $\alpha$  spectrum may inadvertently remove an important piece of evidence in deciphering the origin of the broad emission lines. Given the above considerations, it would seem prudent, albeit novel, to not subtract a narrow H line from any of the Balmer lines seen in NGC 3227, which is the approach adopted here.

The forbidden line model produced using the G750M spectrum is also subtracted from the lower resolution G750L spectrum, motivated by the observation that the flux in the two [S II] lines did not change between 1999 and 2000, with the result that the broad H $\alpha$  emission line flux in the G750L spectrum is  $\sim 11\%$  smaller than measured in the G750M spectrum (see Table 2), presumably a consequence of the aforementioned decrease in the underlying continuum. Figures 3 and 4 illustrate the consequence of subtracting the forbidden [O III]

emission lines from the  $H\beta$  and  $H\gamma$  lines following the procedure described in Devereux (2011b). Emission line fluxes are reported in Table 3 for all the lines that can be reliably resolved and measured in the G430L spectrum including  $H\beta$ ,  $H\gamma$ , the two [O III] vacuum wavelength  $\lambda 4960.30 \text{ \AA}$  and  $\lambda 5008.24 \text{ \AA}$  emission lines. Upper limits are provided for the vacuum wavelength  $\lambda 4364.44 \text{ \AA}$  [O III] emission line and the [O II]  $\lambda\lambda 3727.09, 3729.88$  doublet. The latter is so faint that the [O III]  $\lambda 5008.24$  / [O II]  $\lambda\lambda 3727.09, 3729.88$  emission line ratio measured with STIS locate NGC 3227 outside the boundaries of the Kewley et al. (2006, their Fig. 5) diagnostic diagram. Consequently, the STIS spectra render the AGN in NGC 3227 unclassifiable.<sup>1</sup>

### 2.0.2. Balmer Decrements

The observed Balmer decrements,  $H\alpha/H\beta = 3.96 \pm 0.01$ , slightly lower than the value of  $\sim 5$  reported previously using ground based telescopes (Winge et al. 1995; Cohen 1983), and  $H\beta/H\gamma = 3.15 \pm 0.08$ , measured for the first time with STIS, are both significantly different from the Case B values, 2.75 and 2.1, respectively, in the sense that the observed values are systematically 44% and 50% higher, respectively. Deviations from recombination theory have been noted for other AGNs (e.g., Devereux 2011a,b; Storchi-Bergmann et al., 1997; Bower et al. 1996; Filippenko & Hapern 1984) and have been attributed to collisional excitation in gas of high density and temperature rather than dust extinction. Indeed, the striking similarity between the  $H\alpha$ ,  $H\beta$  and  $H\gamma$  lines illustrated in Figure 5, when they are normalized to their respective peak intensities and the wavelength scales converted to velocity using the non-relativistic Doppler equation, suggests that dust extinction to the BLR in NGC 3227 is negligible.

## 3. BROAD LINE REGION MODELS

NGC 3227 is unable to sustain a radiatively driven outflow (e.g., Fabian, Celotti, & Erlund 2006; King & Pounds 2003; Murry & Chiang 1997; Shlosman, Vitello, & Shaviv 1985) because the AGN radiates at  $\leq 4 \times 10^{-3}$  the Eddington luminosity limit (Winter, Veilleux, McKernan & Kallman 2011; Xu 2011; Vasudevan & Fabian 2009). However, single peak broad Balmer emission lines, similar to those observed in NGC 3227, can be produced by an inflow (e.g., Devereux 2011a) or an accretion disk (e.g., Eracleous & Halpern 2001)

---

<sup>1</sup> The complementary [O I]  $\lambda 6302.04/H\alpha$  emission line ratio can not be quantified as no estimate is provided for the narrow component of the  $H\alpha$  emission line.

and both models are tested in the following.

### 3.1. Central Stellar Mass

In an inflow or disk model the velocity law is determined by the central mass distribution,  $M(r)$ , which can be modeled as a point mass,  $M_{\bullet}$ , representing the BH, embedded in the center of an extended star cluster. The central stellar mass may be important given the relatively low mass estimated for the BH in NGC 3227. Hicks & Malkan (2008) conveniently parameterize the near-infrared,  $1.65\mu$ ,  $H$ -band surface brightness profile of NGC 3227 in terms of a Sérsic function which may be integrated to determine the line-of-sight, or projected, luminosity in a variety of synthetic apertures. Such projected luminosities can be converted into central masses using the mass-to-projected-light ratio provided in Devereux, Becklin & Scoville (1987). Following this methodology leads to the values presented in Table 4 which, when compared to estimates of the central stellar mass density presented previously by Davies et al. (2006, their Figure 15), reveals a very large discrepancy. For example, the first row in Table 4 corresponds to an angular radius of  $\sim 0.01''$  inside which the stellar mass density is estimated to be  $\sim 1.3 \times 10^6 M_{\odot}/\text{pc}^3$ . This is  $\sim 15,000$  times smaller than the value estimated by Davies et al. (2006) inside that same radius. The reason for the difference has not been determined but the impact of the higher stellar mass density on the gas kinematics is substantial, producing higher gas velocities further from the central BH, and altering the shape of the model broad line profile compared to one calculated using the smaller values. Given this difference, the smaller values for the central stellar mass density, presented in Table 4, are adopted in the following analysis.

### 3.2. Inflow and Relativistic Accretion Disk Models

The spherically symmetric inflow model has been described most recently by Devereux (2011a) and simulates a steady-state free-fall of  $\sim 10^4$  *discrete* particles. The velocity law and mass conservation determine the number density of inflowing particles to be  $n(r) \propto r^{-3/2}$ . Consequently, there are only two free parameters; the inner and outer radii of the inflow,  $r_i$  and  $r_o$ , respectively. A cursory exploration of the parameter space revealed that an outer radius,  $r_o = 1.3 \times 10^5 r_g$ , and an inner radius,  $r_i = 9.3 \times 10^3 r_g$ , where  $r_g = GM_{\bullet}/c^2$ , the gravitational radius, produced a reasonable representation of the broad  $H\alpha$ ,  $H\beta$  and  $H\gamma$  lines illustrated in Figure 5.

The relativistic accretion disk model, presented by Chen & Halpern (1989), has been

described most recently by Devereux (2011b). Past experience with this model has revealed that a single peak broad line profile requires a large ratio of outer radius to inner radius, sufficient inclination to produce a symmetrical profile shape, and adequate velocity dispersion to merge the two peaks, a feature of disk models, into a single peak. A cursory search of parameter space yielded a reasonable representation of the Balmer lines illustrated in Figure 5 with a dimensionless outer radius,  $\xi_o = 3.5 \times 10^5 r_g$ , an inner radius,  $\xi_i = 2.5 \times 10^3 r_g$ , an inclination angle measured from the disk normal to the line of sight,  $i = 50^\circ$ , an emissivity law of the form  $r^{-q}$ , where  $q = 2$  and a velocity dispersion for the gas,  $\sigma = 300$  km/s. Interestingly, Figure 5 illustrates that the broad Balmer lines observed with the low resolution gratings can be represented equally well by an inflow or an accretion disk; the reduced  $\chi^2 \sim 8$  for both models. The effective velocity resolution of the model profiles is  $\sim 230$  km/s, similar to that of the G750L grating and about twice that of the G430L grating. In either case the residuals between the observed profiles and the model are  $\leq 10\%$  except for the fainter and consequently noisier  $H\gamma$  line profile. Both the disk and inflow models have a similar shortfall in that they both predict slightly less emission on the blue side of the profile than is observed.

### 3.3. The Importance of Spectral Resolution

Figure 6 shows the broad  $H\alpha$  line measured with the higher resolution G750M grating which reveals a distinctly triangular profile that is easily modeled as an inflow when the model spectrum is binned to  $\sim 27$  km/s, corresponding to the velocity resolution of the G750M grating. On the other hand, the broad  $H\alpha$  line measured with the higher resolution G750M grating is impossible to mimic with an accretion disk model which is expected to resolve two peaks at this higher spectral finesse.<sup>2</sup> Focusing, therefore, on the inflow model, the reduced Chi-squared statistic was computed for 32 values of the outer radius and 18 values of the inner radius in order to constrain the uncertainty on these two parameters. Chi-squared minimum,  $\sim 6$ , coincided with  $r_o = (2 \pm 1) \times 10^5 r_g$ , and  $r_i = (7 \pm 1) \times 10^3 r_g$  which are the parameters adopted to produce the model inflow spectrum shown in Figure 6.

An advantage of modeling the inflow using a Monte Carlo simulation is that it reproduces the small-scale structure, seen in broad emission line profiles, caused by random clumping of particles in radial velocity space. Historically, the widely quoted *optically thick broad line*

---

<sup>2</sup> The broadening parameter in the Chen & Halpern (1989) disk model is not intended to mimic instrumental resolution. Consequently, the model disk spectrum shown in Figure 6 was generated using a non-relativistic Monte Carlo simulation employing a total of  $\sim 10^4$  points. The resulting velocity histogram is binned by 25 km/s and subsequently smoothed using a 40 bin moving average.

*cloud* model found early support by accounting for such irregularities. That model remains popular to this day, even though the origin and confinement of such *clouds* is a major unsolved problem (Mathews & Ferland 1987). With hindsight, it may be more realistic to identify the *clouds* with *filaments*, motivated by the observation that ionized, density bounded gas filaments are commonly seen in the nuclei of active galaxies (Storchi-Bergmann 2009) including the Galactic center (Lacy, Achtermann & Serabyn, 1991). Such filaments have approximately the same gas density and hence the same emissivity regardless of their location with respect to the central AGN, they are optically thin, emit isotropically and have a very low volume filling factor. Consequently, the ionized H gas does not constitute a fluid and is therefore not a Bondi flow (Bondi 1952). As noted by Capriotti, Foltz & Byard (1981), structure in broad line profiles is revealed depending on the number of filaments and the spectral resolution of the detector. The irregularities clearly seen in the broad H $\alpha$  emission line of NGC 3227 observed with the G750M grating are mimicked by the inflow model and suggest that the inflow is illuminated by the collective emission of  $\sim 10^4$  ionized gas *filaments*.

## 4. Discussion

The exquisite spectra obtained for NGC 3227 with the *HST* reveal an important observational phenomenon; that the shape of its bright and broad H $\alpha$  line changes with the resolution of the grating employed to observe it, as expected if the emission line is produced by thousands of discrete emitters as explained previously by Capriotti, Foltz & Byard (1981). Furthermore, the triangular shape observed for the line using the high resolution G750M grating is inconsistent with the profile shape expected for an accretion disk. Whereas it is already known that the velocity field of the narrow line gas in NGC 3227 is chaotic (Walsh et al. 2008, and references therein), the symmetry of the broad H $\alpha$  line suggests a rather ordered velocity field, demonstrably consistent with an inflow, the size, structure and ionization of which is explored further in the following.

### 4.1. Broad Line Region Ionization

The ionizing continuum generated by the AGN in NGC 3227 may be represented, in the year 2000, as a power law with an optical to X-ray spectral index  $\alpha = 1.17$  (Vasudevan & Fabian 2009) and a normalization provided by the extinction corrected UV continuum described in Section 4.2. Integrating the spectral energy distribution from 13.6 eV to 100 keV using the method described previously in Devereux (2011a) predicts  $6.1 \times 10^{52}$  ionizing



ph/s. For comparison, the broad H $\alpha$  emission line flux measured in the year 2000 (Table 2) corresponds to an H $\alpha$  luminosity,  $L(H\alpha) = 2.4 \times 10^7 L_{\odot}$ , which, assuming 45% of the ionizing photons are converted into H $\alpha$  photons (Case B recombination at a temperature of  $10^4$  K), requires  $6.8 \times 10^{52}$  ionizing ph/s using,

$$N_{ion} = L(H\alpha)\alpha_B/\alpha_{H\alpha}^{eff}h\nu_{H\alpha} \quad (1)$$

where  $\alpha_{H\alpha}^{eff} = 1.16 \times 10^{-13} \text{ cm}^3 \text{ s}^{-1}$  is the effective recombination coefficient and  $\alpha_B = 2.59 \times 10^{-13} \text{ cm}^3 \text{ s}^{-1}$  is the total Case B recombination coefficient.

The comparison shows that the number of ionizing photons required to excite the broad H $\alpha$  emission line measured in the year 2000 coincides with the number of ionizing photons available from the AGN in that same year to within  $\sim 10\%$ <sup>3</sup> which is considered to be good, possibly fortuitous, agreement given the large extinction correction and the known UV and X-ray variability (Markowitz et al. 2009; Vasudevan & Fabian 2009). Nevertheless, the comparison suggests that the central AGN is apparently able to ionize the entire BLR in NGC 3227 which necessarily entails a high,  $\sim 100\%$ , covering factor. Even if 44% of the broad H $\alpha$  emission line flux results from collisional excitation, rather than photoionization as alluded to in section 2.0.2, the covering factor is still high  $\sim 62\%$ . Such a high covering factor is easy to achieve with a spherical distribution of gas and impossible to achieve with a thin accretion disk, further favoring an inflow as the origin of the broad Balmer emission lines seen in NGC 3227.

#### 4.2. BLR Size

Kaspi et al. (2005) noted that NGC 3227 does not conform to the correlation between reverberation size and UV luminosity established for quasars and high luminosity AGNs. However, Crenshaw, Kraemer, Bruhweiler, & Ruiz (2001) present evidence for considerable dust extinction to the central UV source in NGC 3227 amounting to  $\sim 4.3$  mag at  $1450\text{\AA}$ . The consequence of matching the extinction corrected  $1450\text{\AA}$  UV luminosity, estimated using Figure 1 to be  $1.68 \times 10^{42} \text{ erg s}^{-1}$ , with the smaller reverberation size measured by Denney et al. (2009, 2010) is to translate NGC 3227 closer to the correlation defined by quasars and high luminosity AGNs thereby reducing the discrepancy first noted by Kaspi et al. (2005).

Adopting a BH mass allows the gravitational radii, constrained using the inflow model

---

<sup>3</sup>independent of the gas density and the filling factor.

(Section 3.3), to be converted into a physical size. If one adopts the reverberation BH mass of  $7.6 \times 10^6 M_\odot$  (Denney et al. 2009, 2010), then the inner and outer radii of the model inflow correspond to  $r_i \sim (3.2 \pm 0.6)$  l.d and  $r_o \sim (89 \pm 36)$  l.d, respectively. Thus, the inner radius of the model inflow consistently coincides with the reverberation radius ( $3.8 \pm 0.8$  l.d.) reported by Denney et al. (2009, 2010). The most straightforward interpretation of this result is that reverberation mapping locates just the inner radius of a much larger volume of ionized gas. Presumably, reverberation mapping locates the inner radius because this is where the number density of inflowing gas filaments is highest and the gas density in the filaments is also highest as explained in Section 4.4, but the emission is inevitably diminished *in a spectrum* to zero intensity for smaller radii by an ever increasing Doppler spread. Thus, the inner radius is actually an illusion. Since the emitting region is ionization bounded, the notion of an outer radius is also an illusion. Consequently, what we perceive as the BLR in NGC 3227, visualized in Figure 7, is just the illuminated shell of a much larger volume of inflowing gas whose actual dimensions remain to be determined. A measure of the inflow rate can be judged from the animation presented in Figure 7 which shows that the inflowing gas takes about 28 weeks to fall from the reverberation radius into the BH.

### 4.3. Photoionization Model

The physical dimensions of the ionized region in NGC 3227 are consistent with the predictions of a photoionization model analogous to the one described for HII regions in Osterbrock & Ferland (2006). In the model, the number of photoionizations is balanced by the number of recombinations at each location in the nebula according to

$$\frac{n_H^o(r) \int_{\nu_T}^{\nu_{max}} N(\nu)_{ion} a(\nu) e^{-\tau(\nu,r)} d\nu}{4\pi r^2} = n_e(r)^2 \alpha_B \quad (2)$$

where  $n_H^o$  is the number density of neutral H atoms,  $n_e$  is the number density of electrons (equal to the number of protons in a pure H nebula), and  $N(\nu)_{ion}$  is the number of ionizing photons per unit frequency,  $\nu$ , characterized previously in section 4.1. The photoionization cross-section,  $a(\nu)$ , presented in Osterbrock & Ferland (2006), is modified to accommodate the consequence of the Doppler effect in diminishing  $a(\nu)$  for infalling H atoms. Specifically, the photoionization cross section for inflowing hydrogen atoms is blue shifted with respect to the central AGN and hence diminished by the strong,  $\nu^{-3}$ , dependence of the photoionization cross section on frequency. The easiest way to visualize this is from the perspective of an inflowing H atom, for which the 13.6 eV ionization edge of the central continuum UV-X-ray source blueshifts to higher frequencies as the H atom accelerates towards the BH. The optical

depth,  $\tau(\nu, r)$ , is computed using

$$\tau(\nu, r) = \int_0^r n_H^o(r) a(\nu) dr \quad (3)$$

and is then substituted into equation 2 and solved for the electron density,  $n_e(r)$ . The integral within each radius is implemented numerically by adopting a distribution  $n_H^o(r) \propto r^{-3/2}$ , identical to that employed to describe the inflow (see section 3.2). The integral over frequency is from the ionization threshold,  $\nu_T$ , (which depends on inflow velocity according to the relativistic Doppler equation) to  $\nu_{max} = 3.29 \times 10^{19}$  Hz. The calculation yields the radial dependence of the electron density,  $n_e(r)$ , the ionization fraction,  $n_e(r)/(n_e(r) + n_H^o(r))$ , and the ionization parameter,  $\Gamma(r)$ , given by

$$\Gamma(r) = N_{ion}/4\pi r^2 c n_e \quad (4)$$

Figure 8 illustrates the radial dependence of these three quantities resulting from photoionization of the neutral gas,  $n_H^o(r)$ . Both the electron density ( $n_e(r) \propto r^{-5/2}$ ) and the ionization fraction ( $\propto r^{-1/2}$ ) increase rapidly *towards* the central AGN leading to the visual impression of a compact BLR. Most of the inflowing gas is completely ionized by the time it reaches the reverberation radius. On the other hand the ionization parameter ( $\Gamma(r) \propto r^{1/2}$ ) increases rapidly *away* from the central AGN to achieve values that are several orders of magnitude larger than those typically employed for BLRs in the literature (e.g., Kwan 1984; Ferland et al. 1992; Lewis, Eracleous & Sambruna 2003; Eracleous, Hwang, & Flohic 2010, and references therein). Values cited in the literature for the ionization parameter are derived, typically, from emission line ratios using photoionization codes (e.g., *Cloudy*, Ferland et al. 1998; Collin-Souffrin & Lasota 1988; Leighly & Casebeer 2007). Thus, there appears to be a large discrepancy between values quoted in the literature for the ionization parameter in BLRs and those implied by the photoionization model presented here. A similar discrepancy has been noted previously by Alexander & Netzer (1994).

#### 4.4. Virial Black Hole Masses

The virial product of reverberation radius,  $R$ , and the velocity width<sup>4</sup> of the broad Balmer line,  $\Delta V$ , leads to a BH mass according to the relation;

---

<sup>4</sup>the FWHM or the second moment (Collin, Kawaguchi, Peterson & Vestergaard 2006).

$$M_{\bullet} = fR\Delta V^2/G \tag{5}$$

where  $f$  is a correction factor that locates the reverberation BH masses on the  $M_{\bullet}-\sigma_*$  relation defined by BH masses measured directly using gas and stellar kinematics.  $f$  has a value of  $\sim 5.5$  (Onken et al. 2004). However, if the broad Balmer lines *are* produced by an inflow then it follows that the reverberation radius corresponds to the inner radius of the flow. Figure 7 visualizes the model inflow and identifies 8% of the broad  $H\beta$  line flux that is observed to be time variable<sup>5</sup> (Winge et al. 1995; Denney et al. 2009, 2010). Figure 9 illustrates that the full width at zero intensity of the broad emission line profile is defined by the inner radius of the inflow. Consequently, the correct virial product, at least for NGC 3227, is the reverberation radius (0.0035 pc) and the half width at zero intensity (4300 km/s) squared. Then one recovers the reverberation BH mass of  $7.6 \times 10^6 M_{\odot}$  with  $f = 1$ . Thus, there is no need for the correction factor,  $f$ , if the virial product utilizes a radius with the maximum velocity measured *at that same radius*.

#### 4.5. Physical Properties of the Inflow

In the context of AGNs, gas inflows have received remarkably little attention in the published literature which is ironic because virtually everyone agrees that AGN activity is fueled by inflowing gas. Single peak broad emission line profiles, which are by far the most common (Strateva et al. 2003), may in particular prove to be a lucrative resource for quantifying the physical properties of gas inflows by providing perhaps the only way to measure a number of key parameters including the mass of emitting gas, the ionized gas volume filling factor and the mass inflow rate. Specific results for NGC 3227 are summarized in Table 5, following the procedure described most recently in Devereux (2011b). An important result is that the observed mass inflow rate,  $\sim 10^{-2} M_{\odot} \text{ yr}^{-1}$ , is commensurate with that required to power the central UV-X-ray source in NGC 3227, assuming radiatively inefficient accretion as parameterized by Merloni, Heinz, & Di Matteo (2003).

Two outstanding conceptual problems remain with regard to fueling AGN. The first is why the accretion rate implied by the bolometric luminosity of the AGN is so low compared to the available gas supply (e.g., Ho 2009). The second unsolved problem is how does the gas lose angular momentum in order to be accreted (e.g., Begelman 1994; Proga

---

<sup>5</sup>The  $H\alpha$  variability amplitude is observed to be  $\sim 11\%$  with STIS. However, adopting 11% of the flux as the time variable component does not change the visual impression depicted in Figure 8 that reverberation mapping locates just the inner edge of a much larger volume of gas.

& Begelman 2003, and references therein). Both of these difficulties can be solved simultaneously if the source of the inflowing material is zero angular momentum gas resulting from stellar-mass loss. Only a small fraction of the stellar mass loss gas is expected to have zero angular momentum but this naturally explains why the accretion rate is observed to be low  $\sim 10^{-2} M_{\odot} \text{ yr}^{-1}$ . Not only is the accretion rate implied by the bolometric luminosity of the AGN low, the accretion rate is *actually observed to be low* and the explanation offered here for that observation is that the BH accretes *only the fraction of gas produced by stellar mass loss that has zero angular momentum*. A corollary of this explanation is that inflowing gas has no rotation; gas with any appreciable angular momentum will not migrate inward for the reasons outlined by Begelman (1994). Thus, inflowing gas, by definition, has no rotation and consequently no angular momentum.

The [S II] lines have a line width corresponding to 360 km/s indicating that they arise from gas at a radial distance of  $\sim 0.5$  pc. Thus, the two [S II] lines provide an opportunity to measure the electron density well beyond the region of the inflow that is ionized by the central AGN. The nominal value for the observed [S II]  $\lambda 6742/\lambda 6757$  intensity ratio =  $0.78 \pm 0.05$ , corresponding to  $n_e = 10^3 \text{ cm}^{-3}$ . The fact that the FWHM of the broad Balmer emission lines is larger than that of the [O I] and [O III] emission lines (Table 2 & 3) suggests that the electron density *inside* the inflow must be greater than the critical density of the levels from which the [O I] and [O III] lines originate which is  $\sim 10^6 \text{ cm}^{-3}$ . This limit is higher than the one obtained from the [S II] line ratio implying that the electron density increases towards the central BH, consistent with the radial dependence predicted by photoionization model (section 4.3).

The vacuum wavelength [O III]  $\lambda 4960.30$  and  $\lambda 5008.24$  lines are observed to have a FWHM  $\sim 800$  km/s, corresponding to a radius of  $\sim 0.1$  pc, providing the opportunity to measure the electron temperature just beyond the outer boundary of the inflow that is ionized by the central AGN. The limit for the observed [O III] ratio ( $\lambda 4960.30 + \lambda 5008.24$ ) /  $\lambda 4364.44 \geq 56$  yields  $T \leq 16,650$  K for the electron temperature if  $n_e = 10^3 \text{ cm}^{-3}$ .

Both Denney et al. (2009) and Winter, Veilleux, McKernan & Kallman (2011) have raised the possibility of outflowing gas *at* and *inside*<sup>6</sup> the reverberation radius in NGC 3227. However, the low Eddington ratio dictates that radiation pressure acting on the ionized gas fails to overcome the gravitational force by a factor of  $\sim 250$ . Furthermore, a dust driven outflow (Fabian, Celotti, & Erlund 2006) seems unlikely as the dust reverberation radius ( $\sim 20$  l.d., Suganuma et al. 2006) lies well beyond the gas reverberation radius ( $\sim 4$  l.d.,

---

<sup>6</sup>Based on the ionization parameter measured for the O VII and O VIII absorption lines by Winter, Veilleux, McKernan & Kallman (2011)

Denney et al. 2009) as illustrated in Figure 7. Additionally, any advection driven outflow is predicted to occur on a size scale comparable to  $r_g$  (Narayan, Kato & Honma 1997) which is  $\sim 1000$  times smaller than the gas reverberation radius in NGC 3227. Thus, it is incumbent on proponents of outflow to identify a viable mechanism that operates over  $4\pi$  steradians and is able to thwart the ballistic pressure of the inflow, estimated to be  $\sim 0.4$  erg/cm<sup>3</sup> at the gas reverberation radius and increasing as  $r^{-2}$  towards the central BH.

#### 4.6. Summary

Collectively, the results presented here for NGC 3227 challenge many preconceived notions concerning the nature of BLRs in active galactic nuclei. Firstly, there are quite likely no *broad line clouds* but rather ionized gas *filaments*. Secondly, the BLR is *not small*, it is just *perceived* to be small. Thirdly, the single peak broad Balmer emission lines, which are by far the most common type of broad emission line seen in AGNs, are quite likely the signature of a sub-parsec sized *ballistic inflow*, not a Bondi flow. Fourthly, the observed mass inflow rate *is* commensurate with that required to power the AGN in terms of radiatively inefficient accretion. However, it remains to be determined to what extent these findings for NGC 3227 apply to more luminous AGNs. Nevertheless, the picture emerging from analysis of *HST*/STIS observations, to date, is that the BLR of LLAGNs are very different from each other with no evidence to support the notion of a *standard, classical or normal* BLR.

### 5. Conclusions

Spectroscopic observations of NGC 3227 with the *Hubble Space Telescope* have revealed a time variable single-peak broad H $\alpha$  emission line profile which has been successfully modeled as a steady state inflow. The *perceived* dimensions of the BLR correspond to an outer radius of  $\sim 90$  l.d. and an inner radius of  $\sim 3$  l.d. that coincides with the gas reverberation radius. However, the *perceived* small size for the BLR is an illusion, a consequence of the fact that the emitting region is ionization bounded at the outer radius and diminished by Doppler broadening at the inner radius. The actual dimensions of the inflow are likely much larger and remain to be determined. If the electron density is high,  $n_e \geq 10^6$  cm<sup>-3</sup>, as suggested by the absence of similarly broad [O I] and [O III] emission lines, then the luminosity in the broad H $\alpha$  emission line observed in the year 2000 leads to a steady state inflow rate  $\sim 10^{-2}$  M $_{\odot}$  yr<sup>-1</sup> which is sufficient to explain the X-ray luminosity of the AGN, if the AGN is powered by radiatively inefficient accretion.

This research has made extensive use of the NASA Astrophysics Data System, the Atomic Line List, <http://www.pa.uky.edu/~peter/newpage/> and a variety **STSDAS** tasks. The author would like to thank Emily Heaton her assistance and the anonymous referee for a thoughtful and charitable report.

*Facilities:* HST (STIS)

## REFERENCES

- Alexander, T., & Netzer, H., 1994, MNRAS, 270, 781
- Begelman, M. C., in Mass-Transfer Induced Activity in Galaxies, proceedings of the Conference held at the University of Kentucky, Lexington, April 26-30, 1993. Edited by Isaac Shlosman. Cambridge: Cambridge University Press, 1994, p.23
- Bondi, H., 1952, MNRAS, 112, 195
- Bower, G.A., Wilson, A.S., Heckman, T.M., & Richstone, D.O., 1996, AJ, 111, 1901
- Capriotti, E., Foltz, C., & Byard, P., 1980, ApJ, 245, 396
- Chen, K., & Halpern, J.P., 1989, ApJ, 344, 115
- Cohen, R.D., 1983, ApJ, 273, 489
- Collin-Souffrin, S., & Lasota, J-P., PASP, 100, 1041.
- Collin, S., Kawaguchi, T., Peterson, B.M., & Vestergaard, M., 2006, *Å*, 456, 75
- Crenshaw, D.M., Kraemer, S.B., Bruhweiler, F.C., & Ruiz, J.R., 2001, ApJ, 555, 633
- Davies, R.I., et al. 2006, ApJ, 646, 754
- Denney, K.D., et al. 2009, ApJ, 704, 80
- Denney, K.D., et al. 2010, ApJ, 721, 715
- Devereux, N., 2011, ApJ, 727, 93
- Devereux, N., 2011, ApJ, 743, 83
- Devereux, N.A., Becklin, E.E., & Scoville, N.Z., 1987, ApJ, 312, 529
- Devereux, N., & Shearer, A., 2007, ApJ, 671, 118
- Edelson, R.A., & Krolik, J.H., 1988, ApJ, 333, 646
- Eracleous, M., & Halpern J.P., 2001, ApJ, 554, 2406
- Eracleous, M., Hwang, J. A., & Flohic, H. M. L. G. 2010, ApJ, 711, 796
- Fabian, A.C., Celotti, A. & Erlund, M.C., 2006, MNRAS, 373, L16
- Ferland et al. 1998, PASP, 110, 761



- Ferland, G.J., et al. 1992, ApJ, 387, 95
- Filippenko, A.V., & Halpern, J.P., 1984, ApJS, 285, 458
- Ho, L.C., 2009, ApJ, 699, 626
- Ho, L.C., Filippenko, A.V., & Sargent, W.L.W., 1995, ApJS, 98, 477
- Ho, L.C., Filippenko, A.V., Sargent, W.L.W., & Peng, C.Y., 1997, ApJS, 112, 391
- Horne, K., Peterson, B., Collier, S., & Netzer, H., 2004, PASP, 116, 465
- Hicks, E.K.S., & Malkan, M.A., 2008, ApJS, 174, 31
- Kaspi, S., Maoz, D., Netzer, H., Peterson, B.M., Vestergaard, M., & Jannuzi, B.T., 2005, ApJ, 629, 61
- King, A., & Pounds, K., 2003, MNRAS, 347, 657
- Kewley, L.J., Groves, B., Kauffmann, G., & Heckman, T., 2006, MNRAS, 372, 961
- Korista, K.T. & Goad, M.R., 2004, ApJ, 606, 749
- Kwan, J., 1984, ApJ, 283, 70
- Lacy, J. H., Achtermann, J. M., & Serabyn, E., 1991, ApJ, 380, 71
- Leighly, K.M., & Casebeer, D., 2007, ASP Conf. Ser., 373, 365
- Lewis, K.T., Eracleous, M., & Sambruna, R.M., 2003, ApJ, 593,115
- Mathews, W.G., & Ferland, G.J., 1987, ApJ, 323, 456
- Merloni, A., Heinz, S., & Di Matteo, T., 2003, MNRAS, 345, 1057
- Markowitz, A., et al., 2009, ApJ, 691, 922
- Murphy, N., & Chiang, J., 1997, ApJ, 474, 91
- Narayan, R., Kato, S., & Honma, F., 1997, ApJ, 476, 49
- Noel–Storr et al. 2003, ApJS, 148, 419
- Onken, C.A., et al. 2004, ApJ, 615, 645
- Osterbrock, D., & Ferland, G. J., 2006, Astrophysics of Gaseous Nebulae and Active Galactic Nuclei, 2nd ed. University Science Books, Sausalito, CA. pg. 23 - 27.

- Pancoast, A., Brewer, B.J., & Treu, T., 2011, *ApJ*, 730, 139
- Peterson, B., 1993, *PASP*, 105, 247
- Peterson, B.M., Crenshaw, D.M., & Meyers, K.A., 1985, *ApJ*, 298, 283
- Peterson, B.M., et al., 2004, *ApJ*, 613, 682
- Proga, D., & Begelman, M.C., 2003, *ApJ*, 592, 767
- Proffitt, C., et al. 2010, *STIS Instrument Handbook, Version 9.0*, (Baltimore: STScI).
- Robinson, A., & Perez, E., *MNRAS*, 244, 138
- Suganuma, M., et al. 2006, *ApJ*, 639, 46
- Shlosman, I., Vitello, P.A., & Shaviv, G., 1985, *ApJ*, 294, 96
- Storchi-Bergmann, *The Monster's Fiery Breath: Feedback in Galaxies, Groups, and Clusters.*  
AIP Conference Proceedings, Volume 1201, pp. 88-91 (2009).
- Storchi-Bergmann, T., Eracleous, M., Ruiz, M.T., Livio, M., Wilson, A. S., Filippenko, A.  
V., 1997, *ApJ*, 489, 87
- Strateva, I.V., et al. 2003, *AJ*, 126, 1720
- Tully, R.B., 1988, *Nearby Galaxies Catalog*, Cambridge University Press.
- Vasudevan, R.V., & Fabian, A.C., 2009, *MNRAS*, 392, 1124
- Walsh, J.L., 2008, *ApJ*, 136, 1677
- Welsh, W.F., & Horne, K., 1991, *ApJ*, 379, 586
- Winge et al., 1995, *ApJ*, 445, 680
- Winter, L.M., Veilleux, S., McKernan, B., & Kallman, T.R., 2011, *ApJ*, 745, 107
- Xu, Y-D., 2011, *ApJ*, 739 64

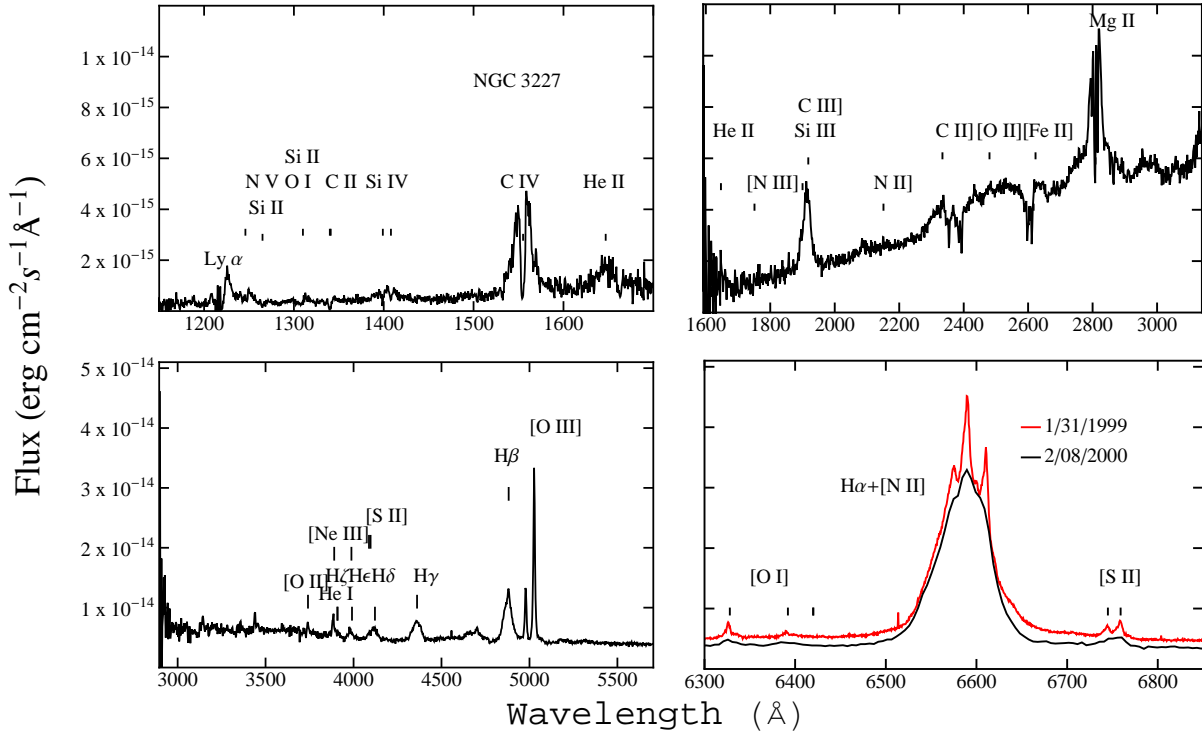


Fig. 1.— Visual and UV spectra of NGC 3227 as seen through the following gratings: *Top left panel:* G140L. *Top right panel:* G230L. *Lower left panel:* G430L. *Lower right panel:* G750M. Red line shows data obtained under PID 7403. Black lines for all panels show data obtained under PID 8479.

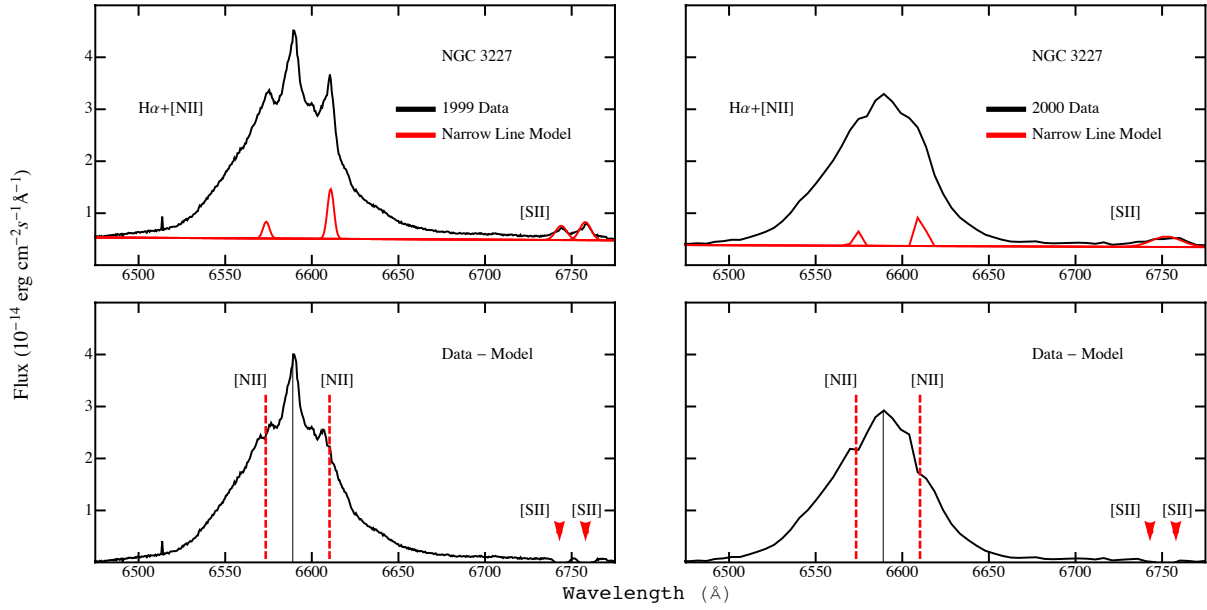


Fig. 2.— Broad  $H\alpha$  emission line in NGC 3227 observed in 1999 with G750M (*Left panels*) and 2000 with G750L (*Right panels*). *Top panels*: The observed spectrum is shown in black and a model for the forbidden lines is shown in red (see also Table 2). *Lower panels*: The broad  $H\alpha$  emission line profile after the forbidden lines have been subtracted. The central wavelengths of the subtracted lines are indicated in red. The vertical black line corresponds to the observed (redshifted) central wavelength of the  $H\alpha$  line

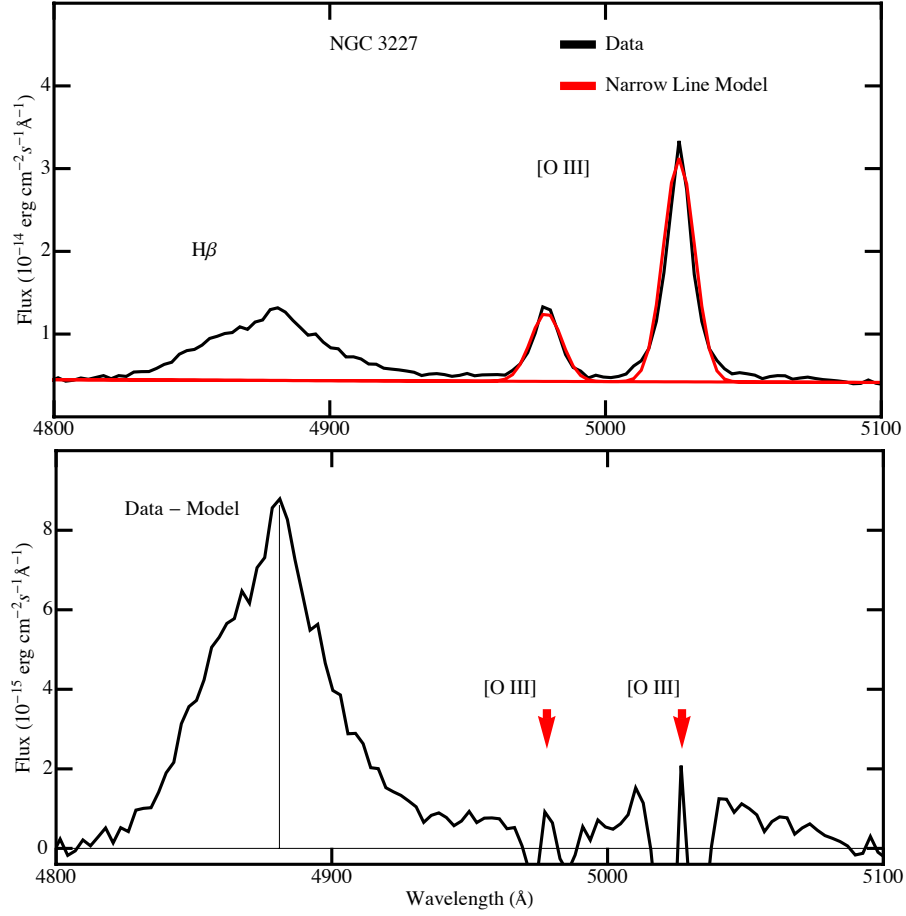


Fig. 3.— Broad H $\beta$  emission line in NGC 3227 observed in 2000. *Top panel:* The observed spectrum is shown in black and a model for the forbidden lines is shown in red (see also Table 3). *Lower panel:* The broad H $\beta$  emission line profile after the forbidden lines have been subtracted. The central wavelengths of the subtracted lines are indicated in red. The vertical black line corresponds to the observed (redshifted) central wavelength of the H $\beta$  line

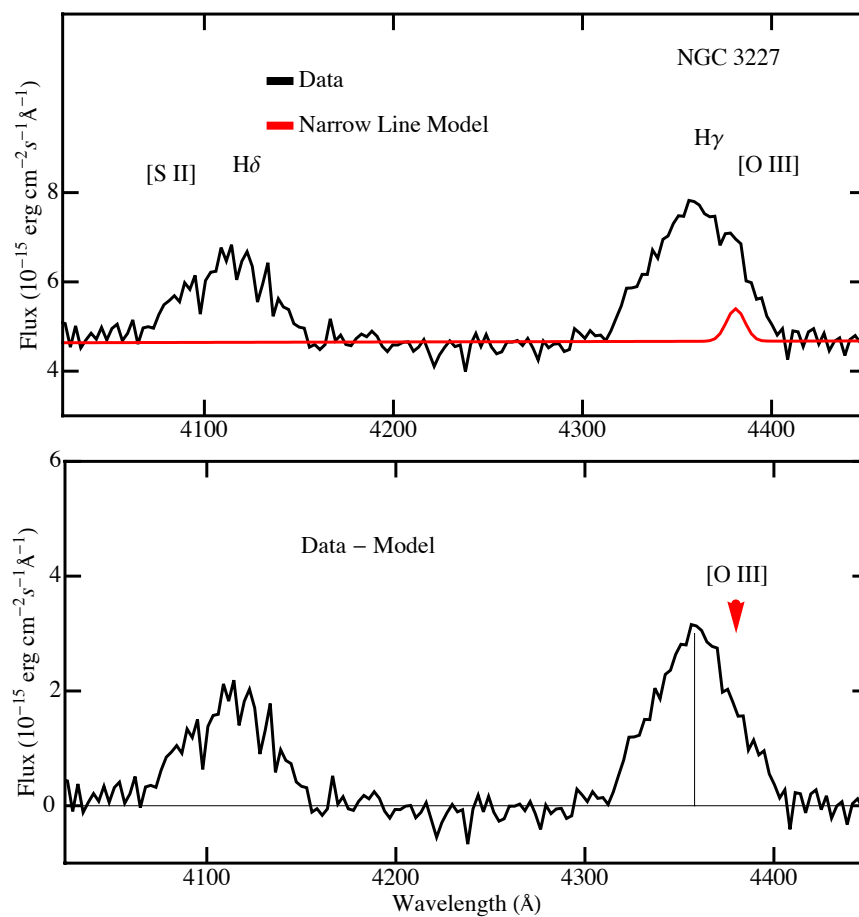


Fig. 4.— Broad H $\gamma$  emission line in NGC 3227 observed in 2000. *Top panel:* The observed spectrum is shown in black and a model for the forbidden line is shown in red (see also Table 3). *Lower panel:* The broad H $\gamma$  emission line profile after the forbidden line has been subtracted. The central wavelength of the subtracted line is indicated in red. The vertical black line corresponds to the observed (redshifted) central wavelength of the H $\gamma$  line

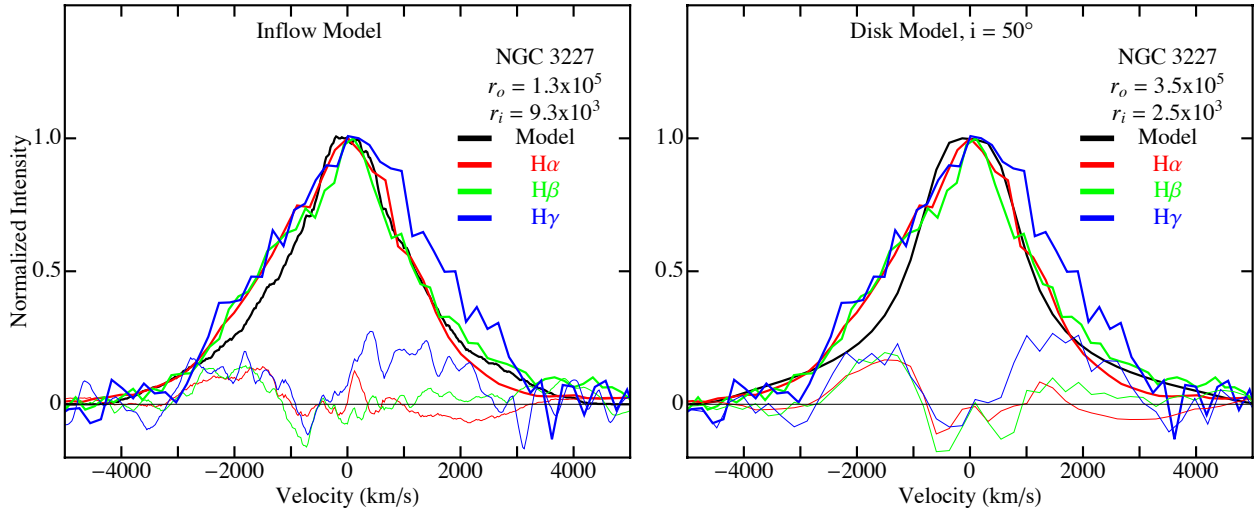


Fig. 5.— Model representation of the broad Balmer lines observed with the G750L grating (Left panel) in terms of a spherically symmetric inflow and (Right panel) in terms of a relativistic accretion disk. The observed  $H\alpha$ ,  $H\beta$  and  $H\gamma$  emission lines are shown in red, green and blue, respectively. The inflow and disk models are shown in black. The inner,  $r_i$ , and outer radii,  $r_o$ , are indicated in units of gravitational radii,  $r_g$ . Residuals for each profile are plotted as thinner colored lines.

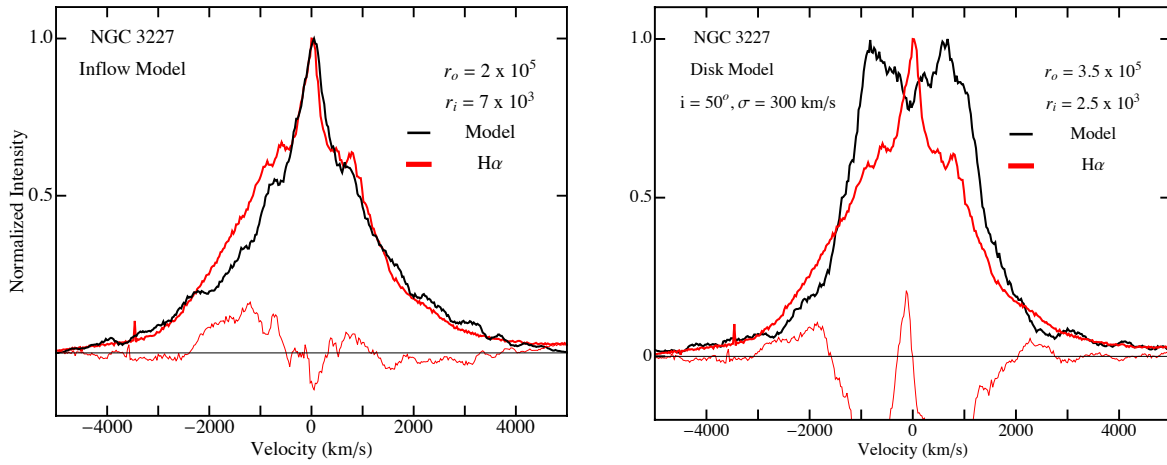


Fig. 6.— Model representation of the broad H $\alpha$  line observed with the G750M grating (Left panel) in terms of a spherically symmetric inflow and (Right panel) in terms of an accretion disk. The observed H $\alpha$  emission line is shown in red. The inflow and disk models are shown in black. The inner,  $r_i$ , and outer radii,  $r_o$ , are indicated in units of gravitational radii,  $r_g$ . Residuals for each profile are plotted as thinner red lines.



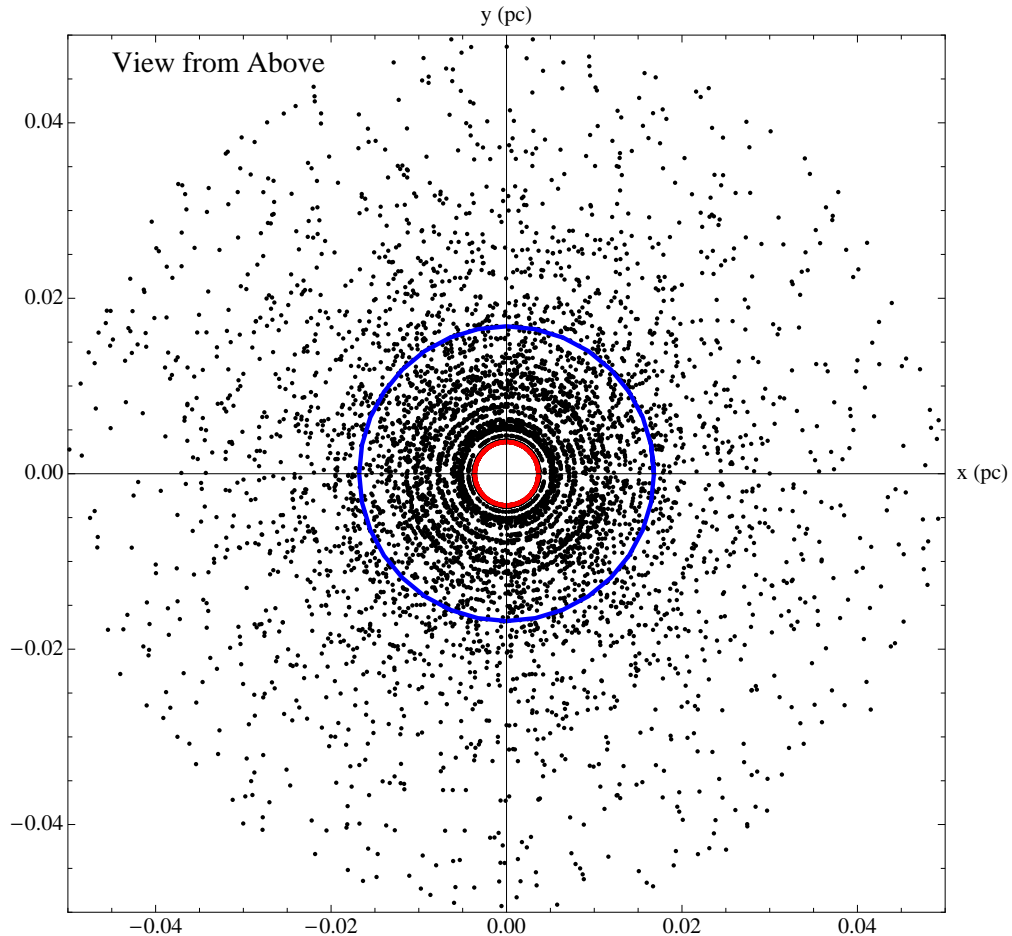


Fig. 7.— Visualization of the model inflow. The red ring identifies 8% of the points representing the percentage of the total broad line flux which is observed to respond to time-variable illumination from the central AGN (Denney et al. 2009, 2010). The blue ring identifies the  $K$ -band reverberation radius (Suganuma et al. 2006). This figure is the first frame in an animation that is accessible in the electronic edition of the *Astrophysical Journal*.

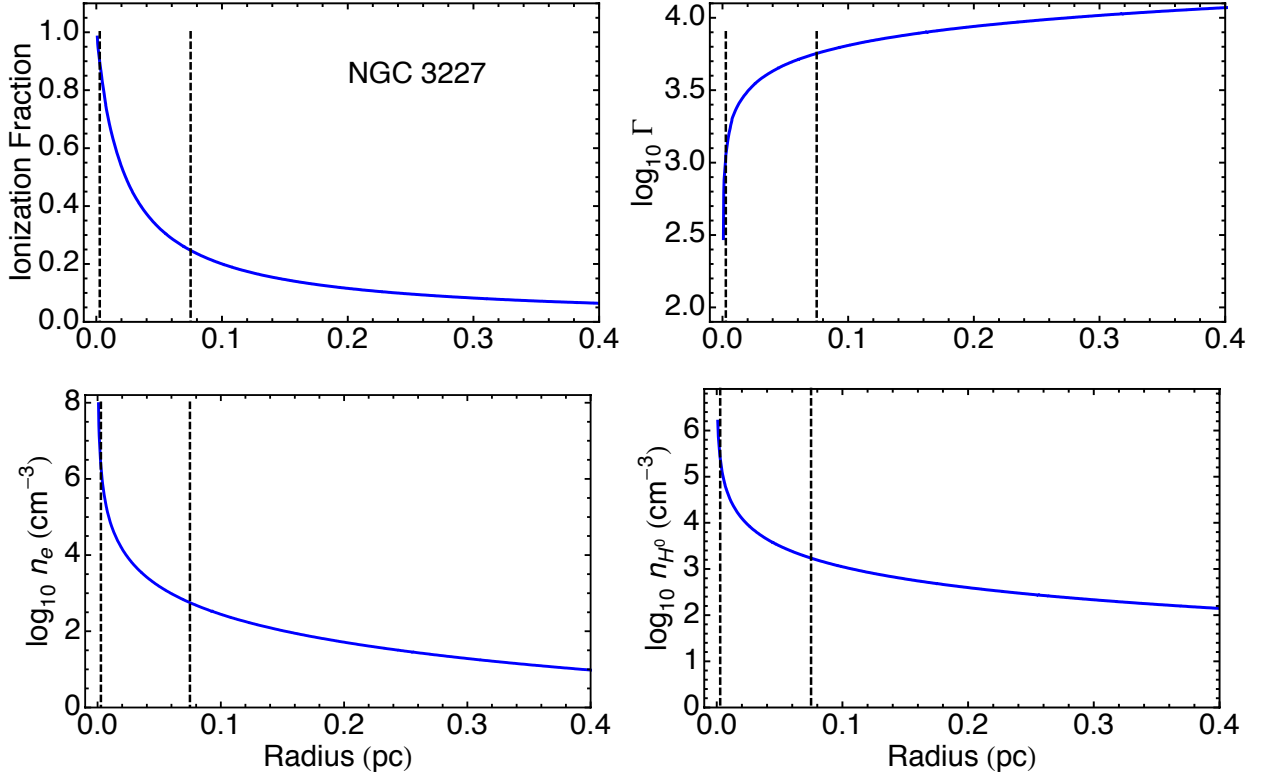


Fig. 8.— Photoionization model results for NGC 3227 illustrating the radial dependence of the ionization fraction,  $\propto r^{-1/2}$  (Top left panel), the ionization parameter,  $\propto r^{1/2}$  (Top right panel), the electron number density,  $\propto r^{-5/2}$  (Lower left panel) and the neutral H number density,  $\propto r^{-3/2}$  (Lower right panel). Vertical dashed lines identify the inner,  $r_i$ , and outer radii,  $r_o$ , of the BLR in units of pc (see section 4.2).

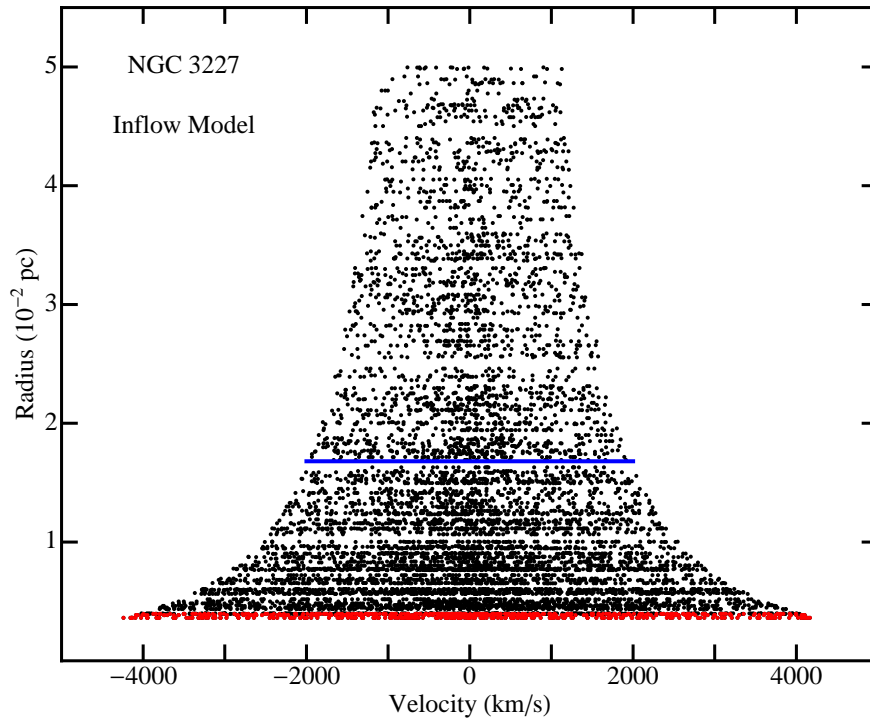


Fig. 9.— The number density of points in the model inflow. Red line identifies 8% of the points representing the percentage of the total broad line flux which is observed to respond to time-variable illumination from the central AGN (Denney et al. 2009, 2010). The blue line identifies the  $K$ -band reverberation radius (Suganuma et al. 2006). The corresponding model broad  $H\alpha$  profiles, shown in Figures 5 and 6, are produced by summing the points vertically.

Table 1. NGC 3227 Spectral Datasets

PID	Observation Date	Grating	Spectral Range Å	Slit arc sec	Dispersion Å/pixel	Plate Scale arc sec/pixel	Integration Time s	Datasets
(1)	(2)	(3)	(4)	(5)	(6)	(7)	(8)	(9)
7403	1-31-1999	G750M	6295 – 6867	52 x 0.2	0.56	0.05	1890	o57204040
8479	2-8-2000	G230L	1570 – 3180	52 x 0.2	1.58	0.025	1612	o5kp01010
8479	2-8-2000	G430L	2900 – 5700	52 x 0.2	2.73	0.05	120	o5kp01020
8479	2-8-2000	G140L	1150 – 1736	52 x 0.2	0.6	0.024	2132	o5kp01030
8479	2-8-2000	G750L	5236 – 10266	52 x 0.2	4.92	0.05	120	o5kp01040

Table 2. Emission Line Parameters for the G750M Nuclear Spectrum Obtained 1–31–1999<sup>a</sup>

Line	Central Wavelength <sup>b</sup> Å	Flux <sup>c</sup> $10^{-15}$ erg cm <sup>-2</sup> s <sup>-1</sup>	FWHM kms <sup>-1</sup>
(1)	(2)	(3)	(4)
[O I]	6326 ± 1	12.9 ± 0.7	298 ± 24
[O I]	6390 ± 1	6.3 ± 0.9	298 ± 52
[N II]	6574 ± 3	15	200
H $\alpha$ (broad) <sup>d</sup>	6588	2200 ± 1	2147 ± 100
H $\alpha$ (broad) <sup>e</sup>	6588	1950 ± 3	2700 ± 200
[N II]	6610 ± 1	45 <sup>f</sup>	200
[S II]	6744 ± 1	20.8 ± 2 <sup>g</sup>	357 ± 47
[S II]	6758 ± 1	26.6 ± 2 <sup>g</sup>	357 ± 34

<sup>a</sup>Table entries that do not include uncertainties are fixed parameters.

<sup>b</sup>Observed wavelength

<sup>c</sup>Measured within a 0.2'' x 0.35'' aperture. Continuum subtracted but not corrected for dust extinction. Model dependent systematic uncertainties introduce an additional ~3% error not reported in the Table.

<sup>d</sup>Observation date: 1–31–1999, G750M

<sup>e</sup>Observation date: 2–8–2000, G750L

<sup>f</sup>The [N II] emission line flux is chosen so as to not over-subtract the broad H $\alpha$  emission line profile.

<sup>g</sup>The [S II] emission lines are unresolved in the lower resolution spectrum obtained with the G750L grating on 2–8–2000. However, the sum of the flux in the two lines then was  $(43.7 \pm 6) \times 10^{-15}$  erg cm<sup>-2</sup> s<sup>-1</sup> which concurs with the sum of the flux in the [S II] lines measured on 1–31–1999 reported in the Table.

Table 3. Emission Line Parameters for the G430L Nuclear Spectrum Obtained 2–8–2000<sup>a</sup>

Line	Central Wavelength <sup>b</sup> Å	Flux <sup>c</sup> $10^{-14}$ erg cm <sup>-2</sup> s <sup>-1</sup>	FWHM kms <sup>-1</sup>
(1)	(2)	(3)	(4)
[O II]	3737 ± 1	≤ 0.6	...
Hγ (broad)	4356	15.6 ± 0.4	3600 ± 300
[O III] <sup>d</sup>	4381	≤ 0.9	778
Hβ (broad)	4882	49.2 ± 0.01	3000 ± 300
[O III]	4978 ± 1	12 ± 1	801 ± 131
[O III]	5027 ± 1	38 ± 2	788 ± 49

<sup>a</sup>Table entries that do not include uncertainties are fixed parameters.

<sup>b</sup>Observed wavelength

<sup>c</sup>Measured within a 0.2'' x 0.35'' aperture. Continuum subtracted but not corrected for dust extinction. Model dependent systematic uncertainties introduce an additional ~3% error not reported in the Table.

<sup>d</sup>The [O III] emission line parameters chosen so as to not over-subtract the broad Hγ emission line profile

Table 4. Stellar Mass Model

r pc (1)	r mas (2)	M(r) <sup>a</sup> 10 <sup>6</sup> M <sub>⊙</sub> (3)	ρ(r) <sup>b</sup> 10 <sup>6</sup> M <sub>⊙</sub> /pc <sup>3</sup> (4)
1	9.90	5.56	1.3
0.5	4.90	1.63	3.1
0.25	2.47	0.48	7.3
0.125	1.24	0.14	16.5
0.0625	0.62	0.04	36.2

<sup>a</sup>Enclosed stellar mass calculated by integrating the *H*-band surface brightness profile parameterized by Hicks & Malkan (2008), adopting an *H*-band mass-to-light ratio M/L = 0.7 and +3.65 for the absolute *H*-band magnitude for the Sun (Devereux, Becklin & Scoville 1987).

<sup>b</sup>Stellar mass density

Table 5. Physical Properties of the Inflow

Parameter (1)	Value (2)
Electron number density, $n_e$	$\geq 10^6 \text{ cm}^{-3}$
H $\alpha$ luminosity <sup>a</sup> , $L(H\alpha)$	$2.4 \times 10^7 L_\odot$
Mass of ionized gas in BLR, $M_{emitting}$	$\leq 222 M_\odot$
Volume filling factor of ionized gas in BLR, $\epsilon$	$\sim 1$
Ionized gas mass inflow rate, $\dot{m}$	$\sim 1.2 \times 10^{-2} M_\odot \text{ yr}^{-1}$
2-10 keV X-ray luminosity <sup>b</sup> , $L_{2-10 \text{ keV}}$	$3.2 \times 10^{41} \text{ erg s}^{-1}$
Mass inflow rate required by AGN, $\dot{m}$	$\sim 1.8 \times 10^{-2} M_\odot \text{ yr}^{-1}$

<sup>a</sup>measured in the year 2000 (Table 2)

<sup>b</sup>measured in the year 2000 (Vasudevan & Fabian 2009)